Performance analysis of a 6U CubeSat ADCS under eclipse conditions with and without gyroscopes measurements

Di Sarno Pietro[1], Fiengo Imma Francesca[2] and Niro Antonio[3]

[1, 2, 3] University of Naples "Federico II", Dept. of Industrial Engineering, Napoli, Italy
[1] pie.disarno@studenti.unina.it
[2] im.fiengo@studenti.unina.it
[3] a.niro@studenti.unina.it

Abstract. Accurate attitude estimation and control are particularly challenging during eclipse conditions, when satellites temporarily lose access to Sun sensors data. This study examines the Attitude Determination and Control System (ADCS) performance of a 6U CubeSat deployed in a Sun-synchronous orbit (SSO). Two distinct ADCS scenarios are evaluated: the first relies exclusively on Sun sensors and magnetometers, while the second integrates gyroscopes measurements. A Multiplicative Extended Kalman Filter (MEKF) and a Proportional-Derivative (PD) controller are utilized to perform attitude estimation and control, respectively. The results indicate substantial performance degradation in the gyroscope-less configuration, with attitude estimation errors significantly exceeding mission tolerances during eclipse phases. Conversely, incorporating gyroscopes markedly enhances pointing accuracy, maintaining errors within acceptable bounds (less than 0.25°) even under challenging eclipse conditions. This highlights the importance of gyroscopic data in maintaining robust ADCS performance during sensor outages.

Keywords. CubeSat, eclipse, Attitude Determination and Control System, Multiplicative Extended Kalma Filter, Proportional-Derivative controller, Sun sensors, magnetometers and gyroscope.

1. Introduction

Optimizing the ADCS for satellites equipped with Sun sensors during eclipse phases is of paramount importance, indeed these periods include significant challenges due to the temporary loss of Sun sensor measurements. During eclipses, satellites experience decreased attitude estimation accuracy, which degrades control performances and consequently compromises mission objectives such as precise Earth observation (EO). This study investigates the ADCS performance of a 6U CubeSat in a 12 AM - 12 PM SSO, employing Reaction Wheels (RWs) and magnetorquers. A PD controller and a MEKF are implemented, first using only Sun sensors and magnetometers, then including gyroscopes measurements. This work aims to enhance the performance of the ADCS during eclipse conditions by integrating gyroscopes data, and to quantitatively assess the improvement in attitude estimation and control accuracy compared to a configuration in which gyroscopes are not available.

The temporary unavailability of Sun sensors measurements during eclipse phases represents a well-documented challenge in satellite attitude determination. Traditional Extended Kalman Filters (EKFs) exhibit significant performance degration under these conditions, prompting the development of algorithms like Expectation-Maximization (EM)-based adaptive EKF [1] and the Laplace Particle Filter integrating Single Value Decomposition (SVD)-based adaptation to measurement noise [2]. These approaches dynamically adjust covariance matrices, substantially improving estimation accuracy and robustness during periods of sensors interruption. Additionally, Hajiyev and Cilden-Guler (2018) emphasized the necessity of including gyroscopes measurements in scenarios where Sun sensors data are unavailable, such as during eclipse phases. Their analysis shows that estimation methods relying only on magnetometers, such as magnetometer-based EKF or prediction-only strategies, lead to significant drift and rapidly decreasing accuracy during extended eclipse periods. They conclude that incorporating gyroscopes is essential to preserve observability and maintain reliable attitude estimation performance when Sun sensors data are missing [3]. Cordova-Alarcon et al. (2014) addressed eclipse conditions by estimating both attitude and angular rates during sunlight phases using Gauss-Newton

method, then propagating both within an EKF framework using only magnetometer data during eclipse. This allowed to avoid using gyroscopes while still maintaining a reasonable level of accuracy [4]. Moreover, the PW-Sat2 CubeSat employed an EKF tailored to maintain attitude estimation performance during sensor outages, such as eclipses, by relying on gyroscopes and magnetometers when Sun sensors data were unavailable [5].

This report studies the performance of an ADCS using only magnetometers and Sun sensors, whose results are shown to be inadequate, and demonstrates that an effective solution is the introduction of a gyroscope.

The present work is organized as follows: Section 2 provides details about the selected 6U satellite and its orbit, as well as the chosen sensors and actuators. Section 3 provides the Guidance, Navigation and Control (GNC) architecture. Section 4 discusses how actuators, sensors and external disturbances are modeled. Section 5 presents the results, demonstrating how the inclusion of gyroscopes improves the overall performance of the system.

2. Scenario

2.1. Spacecraft and mission

The selected mission for this case study is based on the PREFIRE (Polar Radiant Energy in the Far InfraRed Experiment) mission, which employs two identical 6U CubeSats flying in slightly different near-polar, Sun-synchronous, Low Earth Orbits (LEOs). PREFIRE is an EO mission, designed for comprehensive Arctic observation, measuring radiant energy through miniaturized thermal spectrometers to understand Arctic warming mechanisms and their impact on global climate dynamics [6].

For the purpose of this analysis, one of the two PREFIRE CubeSats is considered, in a configuration with deployed solar panels (Figure 1). The dimensions of the 6U structural frame are 300×200×100 mm^3, each deployed solar panel measures 610×200×15 mm^3 with an exposed surface area of 120000 mm^2 and weighs 1.3 kg. The total mass is 12.2 kg, typical for advanced 6U CubeSats with scientific payloads.

This configuration enables realistic modeling of environmental perturbations and of the satellite inertia.
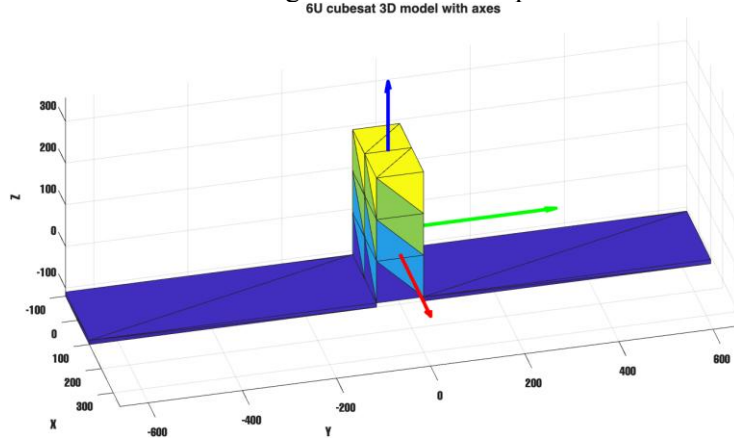

Figure 1: 3D view of selected 6U spacecraft with BRF axes

Component	Value
J_{xx}	$0.6295\ kg\ m^2$
J_{yy}	$0.1644\ kg\ m^2$
J_{zz}	$0.5462\ kg\ m^2$

Table 1: Moments of inertia around BRF axes

The Body Reference Frame (BRF), shown in Figure 1, is centered at the satellite's Center of Mass (CoM), which is at the center of the base face of the main body, 0.118 m above the panels' interface

with the central structure. BRF axes coincide with the satellite's principal axes of inertia. The blue axis represents z_{BRF}, the green axis y_{BRF} and the red axis x_{BRF}. The moments of inertia about these axes are reported in Table 1, the inertia matrix of the satellite $\underline{\underline{J}}$ is a diagonal matrix with the elements corresponding to the values listed in this table.

A three-axis stabilization strategy is adopted, with the BRF aligned with the Orbiting Reference Frame (ORF), defined with the z-axis pointing towards the Earth's centre, the y-axis antiparallel to the orbital angular momentum vector and x-axis to complete the right-handed tern. This choice is consistent with the nature of the mission as an EO platform, which requires the payload to maintain a nadir-pointing configuration.

The orbital scenario has been modified from the original mission parameters to evaluate attitude control performance under alternative and more challenging operational conditions. The selected orbit is a near circular, SSO at 619 km altitude with 97.5° inclination, configured for 12 AM Local Time of Ascending Node (LTAN). This orbital configuration maximizes eclipse duration, representing a worst-case scenario for ADCS performance evaluation where Sun sensors experience extended unavailability. The simulation initiates on July 23, 2025, at 08:30 UTC, covering about four orbital periods totalling 23265 seconds, to allow for comprehensive analysis of attitude control performance across multiple orbital cycles, including several eclipse transitions.

2.2. Sensors and actuators

The Sun sensors measure the direction of the Sun in the BRF, six units are mounted, one on each face of the 6U structure. The magnetometers measure the magnetic field vector in the BRF.

The selected Sun sensors are the CubeSense SunGen 2 units, and the magnetometers are CubeMag Deployable Gen2 units, both provided by CubeSpace [7][8]. The partial obstruction of the Sun sensors' Field Of View (FOV) due to the deployed solar panels is neglected. Each Sun sensor has a FOV of 166° and an angular accuracy σ_{SUN} of 0.1°.

Two magnetometers are used for redundancy, their measurements are provided with an accuracy σ_{MAG} of 16.7 nT along each axis.

Regarding the gyroscopes, the PG400 from ACC Clyde Space is selected. In particular, three units of the gyroscope are considered, arranged along the BRF axes in order to measure the angular velocity of the BRF with respect to the Inertial Reference Frame (IRF), specifically the Earth Centred Inertial (ECI) J2000, expressed in the BRF. PG400 measurements are characterized by a bias term $\underline{b}_g$ of 1 °/h and an Angular Random Walk (ARW) of 0.23 °/$\sqrt{h}$ [9].

These sensors are selected because they are specifically designed for CubeSats and provide acceptable performance in terms of attitude estimation.

The Attitude Control System (ACS) includes 4 RWs and three magnetorquers. The RWs are the CubeWheel CW0057 units from CubeSpace. Their rotational inertia about the spin axes is not explicitly provided in the datasheet, but it has been estimated by dividing the angular momentum at 6 000 RPM by the corresponding angular velocity. The maximum angular speed is 10 000 RPM and the saturation limit is set at 0.8 times this value [10]. These wheels have been selected after evaluating the required torques to control the satellite. The chosen magnetorquers are the NCTR-M003 units from NewSpace Systems, which can provide a maximum magnetic moment of 0.29 Am^2 by adjusting the input current. Additionally, each magnetorquer exhibits a residual magnetic moment of 0.01 Am^2 [11], which is included in the residual magnetic moment of the satellite. Based on [12], the residual magnetic moment of the satellite is set to 0.1 Am^2 along each BRF axis, which is a conservative assumption.

3. GNC Architecture

The GNC architecture developed for this study ensures that the satellite maintains its nominal attitude, defined by alignment of the BRF with the ORF.

The overall architecture, shown in Figure 2, consists of three main blocks: a reference state block, which defines the reference state (guidance); the state estimation block, which estimates the current state using sensors measurements (navigation); and the PD controller (control), which computes the required

torques to track the reference state. The following subsections detail the components of the GNC architecture.
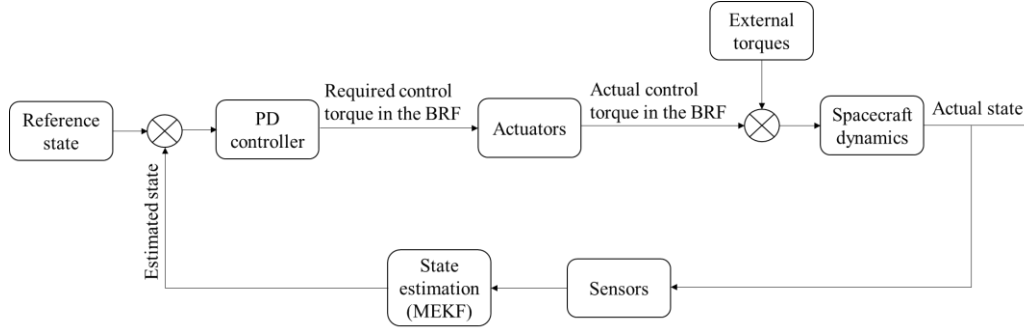

Figure 2: GNC architecture block diagram

3.1. State estimation

Attitude is estimated by means of the MEKF, a tightly coupled architecture is adopted. This enables the state estimation also when the Sun sensors cannot observe Sun direction. The state vector is defined as in Equation (1).

$$\underline{x} = \begin{bmatrix} \boldsymbol{q}_{IB} \\ \omega_{IB}^B \end{bmatrix}_{7\times1} \tag{1}$$

$\boldsymbol{q}_{IB}$ is the unit quaternion defining the attitude of the BRF with respect to the IRF and ω_{IB}^B is the angular velocity, where the apex B indicates that it is expressed in the BRF. The scalar-last convention is used for the quaternion.

The process model in Equation (2) is represented by the kinematic equation for the quaternion and the Euler's equation (neglecting disturbance and control torques) for the angular velocity vector. The time dependency is omitted to ease the notation.

$$\dot{\underline{x}} = \begin{bmatrix} \dot{\boldsymbol{q}}_{IB} \\ \dot{\omega}_{IB}^B \end{bmatrix}_{7\times1} = f(\underline{x}) + \underline{w} = \begin{bmatrix} \frac{1}{2}\omega_{IBq}^B \otimes \boldsymbol{q}_{IB} \\ \underline{\underline{J}}^{-1}\left[-\omega_{IB}^B \times \left(\underline{\underline{J}}\omega_{IB}^B\right)\right] \end{bmatrix} + \underline{w} \tag{2}$$

$\boldsymbol{\omega}_{IBq}^B = \left[\omega_{IB,1}, \omega_{IB,2}, \ \omega_{IB,3}, \ 0\right]^T$ and $\underline{w}$ is the process noise, modelled as zero-mean Gaussian white noise with covariance $\underline{\underline{Q}} = [\ \underline{w}\underline{w}^T]$, i.e., $N\left(0, \underline{\underline{Q}}\right)$.

In the discrete time, being $\underline{x}_{k-1}^+$ the corrected state at the previous time instant $k-1$, the predicted state at the current time instant k, $\underline{x}_k^-$, can be evaluated numerically (Equation (3)) using a discrete version of Equation (2).

$$\underline{x}_k^- = f_d(\underline{x}_{k-1}^+) \tag{3}$$

To satisfy the unit norm constraint of the quaternion, the correction of the state is done as in Equation (4).

$$\underline{x}_k^+ = \begin{bmatrix} \boldsymbol{q}_{IB,k}^+ \\ \omega_{IB,k}^+ \end{bmatrix} = \begin{bmatrix} \delta\boldsymbol{q}_{IB,k} \otimes \boldsymbol{q}_{IB,k}^- \\ \delta\underline{\omega}_{IB,k} + \underline{\omega}_{IB,k}^- \end{bmatrix} \tag{4}$$

The correction on the quaternion is evaluated as a function of $\delta\underline{g}$, which is the correction expressed using the Gibbs vector attitude representation (3 parameters), so that the error covariance matrix $\underline{\underline{P}}$ is not singular.

Introducing the 3-parameters attitude representation, both $\underline{\underline{P}}$ and $\underline{\underline{Q}}$ are 6×6 matrices.

At any time instant the discrete process covariance matrix can be obtained as in Equation (5). Δt is the timespan between instant $k-1$ and k, equal to 1 second.

$$Q_k = \underline{\underline{Q}} \Delta t \tag{5}$$

$\underline{\underline{Q}}$ is given by Equation (6).

$$\underline{\underline{Q}} = \begin{bmatrix} Q_{att}\underline{\underline{I}}_{3\times3} & \underline{\underline{0}}_{3\times3} \\ \underline{\underline{0}}_{3\times3} & Q_\omega\underline{\underline{I}}_{3\times3} \end{bmatrix} \tag{6}$$

Without gyroscopes, the quaternion is propagated with an estimated angular velocity, which is not adjusted by the measurement, so $Q_{att} = 10^{-3}s^{-1}$ to avoid over-confidence of the process. When gyroscopes measurements are available the attitude propagation is more accurate, then $Q_{att} = 10^{-10}s^{-1}$, based on the gyroscopes accuracy (detailed later in this report).

Q_ω has been set equal to the square of the order of magnitude of the external torque ($10^{-12}rad^2/s^3$), which are neglected in the process model, however the final value is $10^{-7}rad^2/s^3$, as better performances in terms of state error have been observed.

The error covariance matrix can be propagated considering Equation (7).

$$\underline{\underline{P}}_k^- = \underline{\underline{\Phi}}_{k-1}\underline{\underline{P}}_{k-1}^+\underline{\underline{\Phi}}_{k-1}^T + \underline{\underline{Q}}_{k-1} \tag{7}$$

The state transition matrix $\underline{\underline{\Phi}}_{k-1}$ can be evaluated as in Equation (8), when Δt is small.

$$\underline{\underline{\Phi}}_{k-1} \cong \underline{\underline{I}} + \underline{\underline{F}}_{k-1}\Delta t \tag{8}$$

$\underline{\underline{F}}$ is the Jacobian of the continuous process model $f(\underline{x})$ at x_{k-1}^+. It is a function of the estimated state, as shown in Equation (9).

$$\underline{\underline{F}}(\widehat{\omega}_{IB}) = \begin{bmatrix} [-\widehat{\omega}_{IB} \times] & \frac{1}{2}\underline{\underline{I}} \\ \underline{\underline{0}} & [-\widehat{\omega}_{IB} \times]\underline{\underline{I}} + [\underline{\underline{I}}\widehat{\omega}_{IB} \times] \end{bmatrix} \tag{9}$$

The Sun sensors and the three-axes magnetometers provide the measured direction in the BRF, $\underline{b}$, of a known inertial vector in the inertial frame, $\underline{r}$(with subscripts S or B to indicate Sun or magnetic field direction, respectively). The gyroscopes directly measure the angular velocity in the BRF. In the case in which the gyroscopes provide measurements, the measurement vector $\underline{y}$ is expressed as in Equation (10).

$$\underline{y} = \underline{h}(\underline{x}) + \underline{v} = \begin{bmatrix} \underline{b}_{S,meas,1} \\ \vdots \\ \underline{b}_{S,meas,s} \\ \underline{b}_{B,meas,1} \\ \underline{b}_{B,meas,2} \\ \omega_{IB,meas}^B \end{bmatrix} = \begin{bmatrix} \underline{\underline{M}}_{IRF\rightarrow BRF}(\boldsymbol{q_{IB}})\underline{r}_S \\ \vdots \\ \underline{\underline{M}}_{IRF\rightarrow BRF}(\boldsymbol{q_{IB}})\underline{r}_S \\ \underline{\underline{M}}_{IRF\rightarrow BRF}(\boldsymbol{q_{IB}})\underline{r}_B \\ \underline{\underline{M}}_{IRF\rightarrow BRF}(\boldsymbol{q_{IB}})\underline{r}_B \\ \omega_{IB}^B \end{bmatrix} + \underline{v} \tag{10}$$

$\underline{y}$ is a $[3(s+2)+3] \times 1$ vector, where s is the number of Sun sensors seeing the Sun at any time instant, 2 is the number of magnetometers and 3 is the number of the three angular velocity components measured by the gyroscopes. It is assumed that all the measurements are available at 1 Hz frequency, equal to the prediction step frequency. $\underline{v}$ is the measurement noise, modelled as zero-mean Gaussian white noise, with covariance $\underline{\underline{R}} = [\underline{v}\underline{v}^T]$, i.e., $N(0,\underline{\underline{R}})$. $\underline{\underline{M}}_{IRF\rightarrow BRF}(\boldsymbol{q_{IB}})$ is the rotation matrix from the IRF to the BRF obtained from the corresponding unit quaternion.

When the gyroscopes are not used $\underline{y}$ is a $3(s+2) \times 1$ vector.

Because the individual sensors are assumed uncorrelated, $\underline{\underline{R}}_k$ is assembled as a block-diagonal matrix whose 3×3 sub-blocks are the variances of the three Cartesian components of each Sun sensor and magnetometer reading; when gyroscopes measurements are available, another 3×3 sub-block is added. For the Sun sensors the manufacturer specifies a 1-σ pointing accuracy of 0.1°[7]. Treating the error as isotropic, each Cartesian component therefore carries the variance reported in Equation (11).

$$R_{SS} = \left(0.1° \cdot \frac{\pi}{180°}\right)^2 = 3.05 \cdot 10^{-6} \tag{11}$$

For the magnetometers the sensor noise is specified in Tesla, while the filter uses the field direction. The Cartesian noise from the datasheet [8] is $\sigma_{mag} = 16.7 \, nT$ and for each magnetometer it is normalized by the norm of the measured magnetic field $\underline{B}_{0,meas}$, The normalisation step amplifies or attenuates the angle error in inverse proportion to the field strength. Hence, for each magnetometer Equation (12) is applied.

$$R_{B,i,k} = \frac{\sigma_{mag}^2}{\left\|\underline{B}_{0,meas,i}\right\|^2} \;, i = 1,2 \tag{12}$$

For the gyroscopes the ARW is $0.23°/\sqrt{h}$ [9], with the measurement frequency at 1 Hz, the variance of the gyroscopes can be evaluated considering Equation (13).

$$R_G = \left(\frac{ARW}{\sqrt{\Delta t}}\right)^2 = \left(0.23 \frac{\pi}{180 \sqrt{3600}} \frac{rad}{s}\right)^2 = 4.48 \cdot 10^{-9} \left(\frac{rad}{s}\right)^2 \tag{13}$$

The resulting expression for $\underline{R}_k$ can be written compactly as in Equation (14). The contribution of the gyroscopes is present or not, depending on the case study.

$$\underline{R}_k = diag\,(\underbrace{R_{SS}\underline{I}_{3\times3}, \dots, R_{SS}\underline{I}_{3\times3}}_{s\ Sun\ sensors}, R_{B,1,k}\underline{I}_{3\times3}, R_{B,2,k}\underline{I}_{3\times3}, R_G\underline{I}_{3\times3}) \tag{14}$$

The Kalmann gain $\underline{K}_k$ at k is computed as in Equation (15).

$$\underline{K}_k = \underline{P}_k^- \underline{H}_k^T \left(\underline{H}_k \underline{P}_k^- \underline{H}_k^T + \underline{R}_k\right)^{-1} \tag{15}$$

$\underline{H}_k$ is the Jacobian of the observation model $\underline{h}(\underline{x})$ evaluated at $\underline{x}_k^-$. When the measurement vector is given by the Sun sensors and magnetometers observations, $\underline{H}_k$ ($3(s+2) \times 6$ matrix) can be expressed as in Equation (16).

$$\underline{H}_k = \begin{bmatrix} \begin{bmatrix} 2\left[\underline{\underline{M}}_{JRF\to BRF}(\boldsymbol{q}_{IB,k}^-)\underline{r}_S \times\right] \\ \vdots \\ 2\left[\underline{\underline{M}}_{JRF\to BRF}(\boldsymbol{q}_{IB,k}^-)\underline{r}_S \times\right] \\ 2\left[\underline{\underline{M}}_{JRF\to BRF}(\boldsymbol{q}_{IB,k}^-)\underline{r}_B \times\right] \\ 2\left[\underline{\underline{M}}_{JRF\to BRF}(\boldsymbol{q}_{IB,k}^-)\underline{r}_B \times\right] \end{bmatrix}_{3(s+2)\times3} & \underline{0}_{3(s+2)\times3} \end{bmatrix} \tag{16}$$

When the gyroscopes measures are available, $\underline{H}_k$ ($[3(s+2)+3] \times 6$ matrix) is expressed as in Equation (17).

$$\underline{H}_k = \begin{bmatrix} \begin{bmatrix} 2\left[\underline{\underline{M}}_{JRF\to BRF}(\boldsymbol{q}_{IB,k}^-)\underline{r}_S \times\right] \\ \vdots \\ 2\left[\underline{\underline{M}}_{JRF\to BRF}(\boldsymbol{q}_{IB,k}^-)\underline{r}_S \times\right] \\ 2\left[\underline{\underline{M}}_{JRF\to BRF}(\boldsymbol{q}_{IB,k}^-)\underline{r}_B \times\right] \\ 2\left[\underline{\underline{M}}_{JRF\to BRF}(\boldsymbol{q}_{IB,k}^-)\underline{r}_B \times\right] \end{bmatrix}_{3(s+2)\times3} & \underline{0}_{3(s+2)\times3} \\ \underline{0}_{3\times3} & \underline{I}_{3\times3} \end{bmatrix} \tag{17}$$

Once the Kalmann gain is known, the innovation is computed and the covariance is updated as shown in Equation (18) and Equation (19), respectively.

$$\begin{bmatrix} \delta g_k \\ \delta\underline{\omega}_{IB,k} \end{bmatrix} = \underline{K}_k \left(\underline{y}_k - \underline{h}(\underline{x}_k^-)\right) \tag{18}$$

$$\underline{P}_k^+ = \left(\underline{I} - \underline{K}_k \underline{H}_k \right) \underline{P}_k^-$$

(19)

The attitude correction in terms of quaternion error can be evaluated using Equation (20).

(20)

$$\delta \boldsymbol{q}_{IB,k} = \frac{\left[\delta \underline{g}_k, 1 \right]^T}{\sqrt{1 + \delta \underline{g}_k^T \delta \underline{g}_k}}$$

Finally, the state is updated considering Equation (4).

To initialize the filter, an initial state estimation $\underline{x}_0 = \left[\boldsymbol{q_0}, \underline{\omega}_0 \right]^T$ and an initial state estimation error covariance $\underline{P}_0$ are needed. At the initial instant the satellite is at an argument of latitude of 90°, it is not in eclipse and the magnetic field and Sun direction are not parallel, thus the QUEST solution is computed from the very first set of Sun-sensor and measurements vectors, delivering both the quaternion q_0^{QUEST} and the 3×3 covariance $\underline{P}_{\delta\theta}$ of the associated rotation vector $\delta\underline{\theta}$. Because the MEKF represents attitude errors through $\delta\underline{g} = \frac{1}{2}\delta\underline{\theta}$, the QUEST covariance is scaled accordingly, as shown in Equation (21).

(21)

$$\underline{P}_{\delta g} = \frac{1}{4}\underline{P}_{\delta\theta}$$

The angular velocity component along y_{BRF} is set equal to the orbital mean motion (the other two are set to 0), under the assumptions that detumbling has already been performed and the BRF is aligned with the ORF. An angular velocity error variance of $10^{-7} rad^2/s^2$ is assumed.

Finally, the complete initial state and covariance are assembled as shown in Equation (22).

(22)

$$\underline{x}_0 = \begin{bmatrix} q_0^{QUEST} \\ \underline{\omega}_{orb} \end{bmatrix}, \quad \underline{P}_0 = \begin{bmatrix} \underline{P}_{\delta g} & \underline{0}_{3\times3} \\ \underline{0}_{3\times3} & 10^{-7} \cdot \underline{I}_{3\times3} \end{bmatrix}$$

3.2. Attitude control

The attitude control is based on a PD controller, the required control torque, $T_{c,i}$, around each axis of the BRF is computed assuming 3 separated second-order systems (Equation (23)). Let $\theta_i \in \{\alpha, \beta, \gamma\}$ denote roll, pitch and yaw angles, defining the attitude of the BRF with respect to the ORF by means of a 321 rotation $(\underline{M}_{ORF \rightarrow BRF} = M_1(\alpha)M_2(\beta)M_3(\gamma))$. Under the small angles assumption these can be considered the rotations around the x_{BRF}, y_{BRF} and z_{BRF} axes, respectively. J_{ii} is the satellite inertia about the i-th axis of the BRF, $T_{ext,i}$ is the disturbance torque acting on the i-th axis ($i = x_{BRF}$, y_{BRF}, z_{BRF}). $\theta_{i,ref}$ is the commanded value of the attitude angle, which is 0 for roll, pitch and yaw since the nominal attitude is BRF aligned with ORF. $K_{p,i}$ and $K_{d,i}$ are the proportional and derivative gains, respectively. The control logic for each axis is schematized in Figure 3.
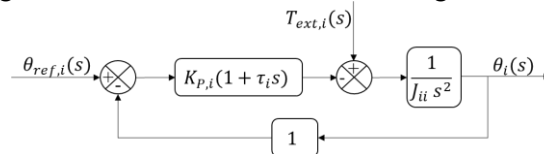

Figure 3: Single axis control logic block diagram in the state space

(23)

$$J_{ii}\ddot{\theta}_i + \underbrace{K_{d,i}\frac{d}{dt}\left(\theta_i - \theta_{i,ref}\right) + K_{p,i}\left(\theta_i - \theta_{i,ref}\right)}_{-T_{c,i}} = T_{ext,i}$$

Equation (23) assumes zero initial conditions and unitary feedback, i.e., perfect knowledge of the state variables. In the actual system implementation, the control torques are computed based on the estimated attitude and angular velocity provided by the MEKF. The controller gains have been first computed imposing for θ_i a steady state value $\theta_{i,ss}$, obtained increasing of one order of magnitude the attitude determination errors in nominal conditions (no eclipse and magnetic field not aligned with Sun direction) on each angle. The proportional gain is evaluated as in Equation (24), considering the presence of a step-like torque with an amplitude equal to the maximum torque along the axis (this is a conservative assumption).

$$K_{P,i} = \frac{T_{ext,max,i}}{\theta_{i,ss}} \tag{24}$$

To have critical dumping, the relation between $K_{P,i}$ and the system time constant τ_i, expressed in Equation (25), must be satisfied.

$$\tau_i = \sqrt{\frac{4\,J_{ii}}{K_{P,i}}} \tag{25}$$

In the end, the derivative gain can be evaluated as in Equation (26).

$$K_{d,i} = K_{p,i}\tau_i \tag{26}$$

The results obtained using this methodology are shown in Table 2 both for the cases with and without gyroscopes.

Axis	Gyroscope-less case			Gyroscope-assisted case		
	Roll	Pitch	Yaw	Roll	Pitch	Yaw
Steady state value (°)	0.20	0.30	0.50	0.15	0.20	0.20
$T_{e,max,i}$ (Nm)	$5.30 \cdot 10^{-6}$	$5.77 \cdot 10^{-6}$	$2.93 \cdot 10^{-6}$	$5.30 \cdot 10^{-6}$	$5.77 \cdot 10^{-6}$	$2.93 \cdot 10^{-6}$
$K_{p,i}$ (Nm)	0.0015	0.0011	0.00036	0.0020	0.0017	0.00084
$K_{d,i}$ (Nms)	0.062	0.027	0.027	0.071	0.033	0.043

Table 2: PD controller gains evaluation results

For the gyroscope-less case, after manual tuning, the selected proportional gains for roll and pitch are $0.00076\ Nm$ and $0.00028\ Nm$, while the derivative gains are set at $0.044\ Nm$s (roll) and $0.019\ Nm$s (pitch). For the gyroscope-assisted case the selected K_p for roll and yaw are $0.0036\ Nm$ and $0.084\ Nm$, respectively.

Finally, the coupled roll-yaw dynamics has been checked by analysing the fourth-order characteristic polynomial that includes cross-coupling terms. All poles remain in the open left half-plane, confirming that the PD design is stable for both gyro-assisted and gyro-less operating modes. The actual implementation of the controller, shown in Figure 4, reflects the separation of the PD control logic along the three BRF axes, it takes as input the estimated angular velocity in the BRF frame and the Euler's angles representing the ORF-to-BRF orientation (evaluated starting from the estimated quaternion).
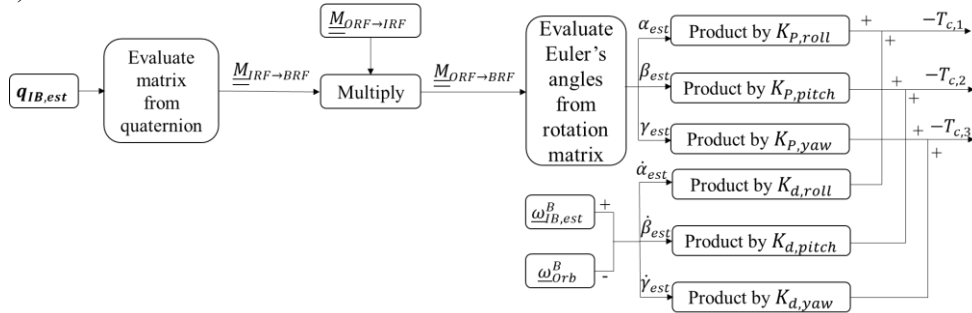

Figure 4: PD controller block diagram

4. Simulation Environment

4.1. Actuators model

The 4 selected RWs are configured in a tetrahedral layout. The magnetorquers are arranged with their axes $\hat{\underline{n}}_i$ (with i = 1, 2, 3) aligned with the axes of the BRF, as shown in Figure 5, where the wheels are numbered from 1 to 4 and their relative positioning with respect to the BRF is illustrated.
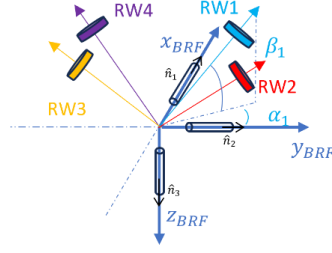
Figure 5: Reaction wheels and magnetorquers with respect to the BRF

The angles between the i-th wheel axis and the xy plane of the BRF, as well as the angle between the projection of the wheel axis on the xy plane and the y axis are defined as the installation angles β_i and α_i respectively, and are both set equal to 45° for each wheel.
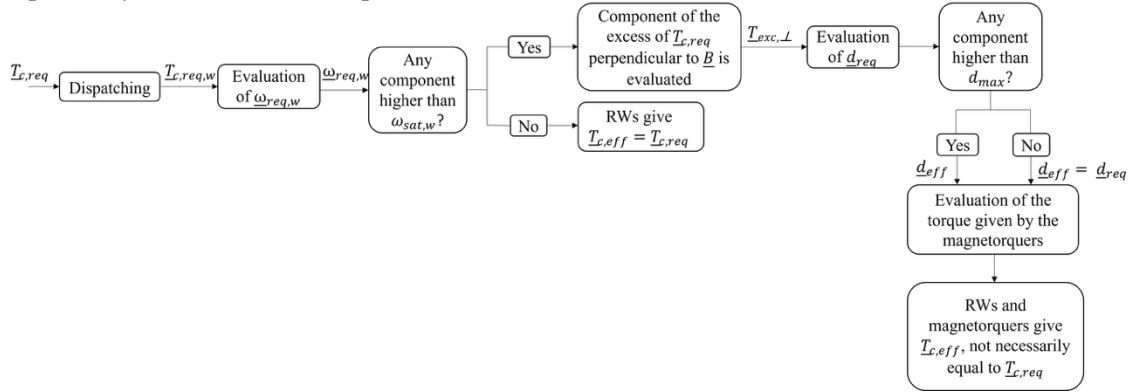

Figure 6: Actuators block diagram

The actuator block has been implemented in the MATLAB Simulink environment, following the logic shown in Figure 6: the torque $\underline{T}_{c,req}$ required to control the satellite is given as input. This torque is distributed across the four RWs through the left pseudo-inverse of the actuation matrix $\underline{A}_{ww}$, obtaining $\underline{T}_{c,req,w}$ as expressed in Equation (27):

$$\underline{T}_{c,req,w} = pinv(\underline{A}_{ww})\underline{T}_{c,req} \tag{27}$$

where $\underline{A}_{ww}$ is defined as in Equation (28).

$$\underline{A}_{ww} = \begin{bmatrix} \cos(\beta_1)\sin(\alpha_1) & -\cos(\beta_2)\sin(\alpha_2) & -\cos(\beta_3)\sin(\alpha_3) & \cos(\beta_4)\sin(\alpha_4) \\ \cos(\beta_1)\cos(\alpha_1) & \cos(\beta_2)\cos(\alpha_2) & -\cos(\beta_3)\cos(\alpha_3) & -\cos(\beta_4)\cos(\alpha_4) \\ -\sin(\beta_1) & -\sin(\beta_2) & -\sin(\beta_3) & -\sin(\beta_4) \end{bmatrix} \tag{28}$$

The angular velocity that each wheel must reach to generate the required torque, $\underline{\omega}_{req,w}$ is computed by integrating the angular acceleration of the wheels, obtained from $\underline{T}_{c,req,w}$. If the required angular velocity of all the RWs does not exceed the saturation threshold $\omega_{sat,w}$, then RWs provide $\underline{T}_{c,eff}$ which is exactly equal to $\underline{T}_{c,req}$. If the angular velocity of at least one wheel exceeds the value of $\omega_{sat,w}$, the wheels are unable to provide the full $\underline{T}_{c,req}$ and there is an excess torque $\underline{T}_{exc}$. In this case, $\underline{T}_{exc}$ is partially supplied by the magnetorquers, which are able to deliver only torque component that is perpendicular to the Earth's magnetic field $\underline{B}_0$. In fact, the torque generated by the magnetic torquers $\underline{T}_{mag}$ is given by Equation (29):

$$\underline{T}_{mag} = \underline{d} \times \underline{B}_0 \tag{29}$$

where $\underline{d}$ is the magnetic moment vector generated by the magnetorquers. The perpendicular component of the excess torque is computed as in Equation (30) where $\hat{\underline{B}}_{0,meas}$ is the magnetic field direction measured by the magnetometers (assumed to be located at the satellite's CoM).

$$\underline{T}_{exc,\perp} = \underline{T}_{exc} - (\hat{\underline{B}}_{0,meas} \cdot \underline{T}_{exc})\hat{\underline{B}}_{0,meas} \tag{30}$$

The obtained value of $\underline{T}_{exc,\perp}$ represents the torque required from the magnetic actuators. It is then possible to compute the required magnetic moment $\underline{d}_{req}$, assuming that it is perpendicular to $\underline{\hat{B}}_{0,meas}$ (the satellite has three magnetorquers along the three axes of the BRF, so it is possible to get $\underline{d}$ along any direction) following Equation (31):

$$\underline{d}_{req} = \frac{\underline{B}_{0,meas} \times \underline{T}_{exc,\perp}}{B_{0,meas}^2} \qquad (31)$$

$\underline{d}_{req}$ has 3 components, which are the magnetic moments required for each magnetorquer. If any value exceeds the maximum specified in the datasheet [11], it is set equal to that maximum, then $\underline{d}_{eff}$ is the effective magnetic moment. The magnetic torque actually provided by the magnetic actuators is computed according to Equation (29), where $\underline{d} = \underline{d}_{eff}$ and it is summed to the torque provided by the RWs.

In this case, $\underline{T}_{c,eff}$ provided by the actuators is generally not equal to $\underline{T}_{c,req}$. In fact, there is still a residual component since magnetorquers can only generate the torque component $\underline{T}_{exc,\perp}$ and not the one parallel to $\underline{\hat{B}}_0$ (assuming that the required magnetic moment does not exceed the maximum allowed).

$\underline{T}_{c,eff}$ provided by the actuators is used as input to Euler's equation to propagate to the next time step, according to Equation (32), which describes the rotational motion of the satellite with respect to the BRF.

$$\underline{\underline{J}}\underline{\dot{\omega}}_{IB}^B = -\underline{\omega}_{IB}^B \times \left(\underline{\underline{J}}\underline{\omega}_{IB}^B + \underline{h}_w\right) + \underline{T}_{c,eff} + \underline{T}_{ext} \qquad (32)$$

$\underline{h}_w$ is the angular momentum of the wheels and $\underline{T}_{ext}$ is the sum of the external torques acting on the satellite.

4.2. Sensors model

To simulate the Sun sensors measurements, the first step is to check if the satellite is in eclipse. If it is in shadow, the Sun sensors do not provide any measurements. Otherwise, the sensors that can see the Sun are identified.
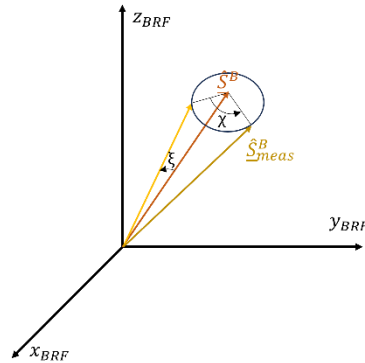

Figure 7: Measurement error simulation for the Sun direction

The true direction vector from the satellite to the Sun, expressed in the BRF, is denoted as $\hat{\underline{S}}^B$. The measured direction of each sensor in BRF is then derived by considering an angular separation ξ from $\hat{\underline{S}}^B$. ξ represents the angular error in the sensor's measurement and is drawn from a zero-mean Gaussian distribution with a standard deviation of 0.1°, as specified in the sensor's datasheet[7]. Specifically, the measurement $\hat{\underline{S}}_{meas}^B$ is assumed to lie on the surface of a cone with axis aligned with $\hat{\underline{S}}^B$ and aperture angle ξ. The specific location on the cone surface is established by an additional rotation by an angle χ, drawn from a uniform distribution over the interval $[0, 2\pi]$, since the probability of lying along any given direction on the cone is the same for all directions (Figure 7).

For the magnetometers, starting from the true components of the magnetic field in the BRF, $\underline{B}_0^B$, evaluated at the satellite's CoM, a noise term is added to each component. This noise is sampled from a

zero-mean Gaussian distribution with a standard deviation equal to 16.7 nT (as specified in the datasheet [8]).

The resulting perturbed components represent the measured magnetic field vector, $\underline{B}^B_{0,meas}$ which is then normalized to obtain the measured direction of the magnetic field $\underline{\hat{B}}^B_{0,meas}$.

To model the gyroscopes angular velocity measurements,two disturbance terms are added to $\underline{\omega}^B_{IB}$: a constant bias $\underline{b}_g = [4.8 \quad 4.8 \quad 4.8]^T \cdot 10^{-6} \frac{rad}{s}$ and a Gaussian white noise $\underline{\eta}_g$,which models the ARW effect, accounting for the random error introduced by sensor noise in the angular velocity measurements. To simulate this noise in the MATLAB Simulink discrete-time system with time step of 1 second, the three components of $\underline{\eta}_g$ are obtained from the sampling of a zero-mean Gaussian distribution with standard deviation σ, which is expressed in Equation (33):

$$\sigma = \frac{ARW}{\sqrt{dt}} = 6.7 \cdot 10^{-5} \frac{rad}{s} \tag{33}$$

The angular velocity $\underline{\omega}^B_{IB,meas}$ measured by the gyroscope is obtained as shown in Equation (34).

$$\underline{\omega}^B_{IB,meas} = \underline{\omega}^B_{IB} + \underline{b}_g + \underline{\eta}_g \tag{34}$$

4.3. Environmental disturbance models

The aerodynamic drag acceleration $\underline{a}^{ECI}_{drag}$ acting on the spacecraft is modeled according to the standard drag equation (Equation (35)):

$$\underline{a}^{ECI}_{drag} = -\frac{1}{2} \frac{C_d A}{m} \rho_{atm} \left|\left|\underline{v}^{ECI}\right|\right|^2 \hat{\underline{v}}^{ECI} \tag{35}$$

Where ρ_{atm} is is the atmospheric density computed using the NRLMSISE-00 atmospheric model, which provides accurate density estimates as a function of altitude, solar activity, and geomagnetic conditions [13]. The drag coefficient used for the selected configuration is $C_d = 2.2$ [14], A is the spacecraft cross-sectional area exposed to the atmospheric flow, m is the total spacecraft mass, v^{ECI} is the velocity vector in ECI and $\hat{v}^{ECI}$ is the corresponding unit vector. The spacecraft is discretized into multiple volumetric elements to accurately account for the torque generated by aerodynamic forces acting off-center relative to the spacecraft's CoM. For each discrete element i with surface area A_i exposed to the atmospheric flow, the local torque contribution is computed as in Equation (36).

$$\underline{T}^{ORF}_{Aero,i} = \frac{1}{2} C_d A_i \left(\underline{u}^{ORF}_w \times \underline{c}^{ORF}_{p,i}\right) \tag{36}$$

Where $\underline{u}^{ORF}_w$ represents the wind direction, expressed in ORF, and $\underline{c}^{ORF}_{p,i}$ is the position vector from the spacecraft center of mass to the center of pressure of element i, expressed in the ORF. The total aerodynamic torque is obtained by integrating contributions from all exposed elements: $\underline{T}^{ORF}_{Aero} = \Sigma_i \underline{T}^{ORF}_{Aero,i}$. This value is then expressed in the BRF by means of the correspondant rotation matrix. The geometric discretization algorithm accounts for shadowing effects and variable surface orientations relative to the velocity vector, which is particularly important for spacecraft with extended solar panels that experience significant attitude-dependent drag variations.

The Solar Radiation Pressure (SRP) disturbance torque is modeled when the spacecraft is in sunlight conditions. The spacecraft geometry is discretized into ten distinct surfaces, 6 for the CubeSat body and 4 for the upper and lower faces of the two deployed panels. The Center of Pressure (CoP) for each surface is considered to be located at the geometric center of the respective face. The position vectors from the center of mass to each CoP ($\underline{r}^B_{cp,i}$) are defined in the BRF. Table 3 summarizes the surfaces areas and $\underline{r}^B_{cp,i}$.

Surface	Area	r^B_{cp} (m)
+Z face	$0.02 \, m^2$	[0, 0, 0.190]
-Z face	$0.02 \, m^2$	[0, 0, -0.110]

+Y face	$0.06\ m^2$	[0, 0.050, 0.040]
-Y face	$0.06\ m^2$	[0, -0.050, 0.040]
+X face	$0.03\ m^2$	[0.100, 0, 0.040]
-X face	$0.03\ m^2$	[-0.100, 0, 0.040]
±Z, +Y Solar Panel (both faces)	$0.122\ m^2$	[0, 0.355, 0.110]
±Z, -Y Solar Panel (both faces)	$0.122\ m^2$	[0, -0.355, 0.110]

Table 3: Surfaces data for SRP torque calculation

The solar panel CoPs are located at [0,±0.355, 0.110] m, reflecting their extended positions along the ±Y axes from the spacecraft CoM. The reflectivity coefficients are differentiated based on surface material properties and functionality. Eight surfaces (all CubeSat body faces and the solar panel undersides) employ a standard coefficient $C_r = 1.5$, representing typical spacecraft surface materials. The two active solar panel surfaces (those facing the -Z direction) utilize a coefficient $C_r = 1.0$ to account for their photovoltaic cell properties and enhanced reflective characteristics [14]. For each surface i, the solar incidence angle θ is determined by computing the dot product between the Sun direction vector $\hat{\underline{S}}^B$ and the surface normal using: $\cos(\theta_i) = \hat{\underline{S}}^B \cdot \hat{\underline{n}}_i$. The surface is considered illuminated only if $\cos(\theta_i) > 0$, ensuring that shadowed or back-facing surfaces do not generate spurious forces. For illuminated surfaces, the SRP force magnitude is calculated as in Equation (37).

$$F_{SRP,i} = P_{sun} A_i C_{r,i} \cos(\theta_i) \qquad (37)$$

where P_{sun} is the solar pressure constant at 1 Astronomical Unit (AU), A_i is the surface area, $C_{r,i}$ is the reflectivity coefficient, and θ_i is the angle between the surface normal and the Sun direction vector. The SRP force $\underline{F}^B_{SRP,i}$ is then multiplied for $\hat{\underline{n}}_i$ to obtain the SRP force vector. The total SRP torque is obtained as in Equation (38) by summing the moments generated by all illuminated surfaces about the spacecraft CoM, considering $\underline{r}^B_{cp,i}$ the position vector from the spacecraft CoM to the center of pressure of the i-th surface:

$$\underline{T}^B_{SRP} = \sum_{i=1}^{10} \underline{r}^B_{cp,i} \times \underline{F}^B_{SRP,i} \qquad (38)$$

The gravity gradient torque is computed as in Equation (39).

$$\underline{T}^B_{gg} = 3\, \frac{\mu}{||\underline{r}^B||^3}\, \hat{\underline{r}}^B \times \left(\underline{\underline{J}} \cdot \hat{\underline{r}}^B \right) \qquad (39)$$

where μ is Earth's gravitational constant, $\underline{r}^B$ is the position vector expressed in BRF and $\hat{\underline{r}}^B$ the corresponding unit vector. For the 6U CubeSat configuration with deployed solar panel, this torque tends to align the spacecraft's minimum inertia axis with the local vertical, generating continuous disturbances in the range of 10^{-6} to 10^{-5} N·m. The asymmetric inertia distribution due to the extended solar panel configuration amplifies the gravity gradient effect, requiring continuous compensation by the attitude control system.The magnetic disturbance torque acting on spacecraft is computed as in Equation (40)

$$\underline{T}^B_{mag} = \underline{m}^B \times \underline{B}^B_0 \qquad (40)$$

where $\underline{m}^B$ represents the spacecraft's magnetic dipole moment, $\underline{B}^B_0$ is calculated from the International Geomagnetic Reference Field (IGRF) model. The IGRF employs spherical harmonic expansion with Schmidt semi-normalized associated Legendre polynomials [15]. The algorithm recursively calculates associated Legendre polynomials and trigonometric terms based on the spacecraft position in Earth-centered coordinates. These polynomials are combined with Gauss coefficients to build the three magnetic field components. Figure 8 shows the total disturbance torque acting on the controlled spacecraft when including gyroscopes measurements in the MEKF.
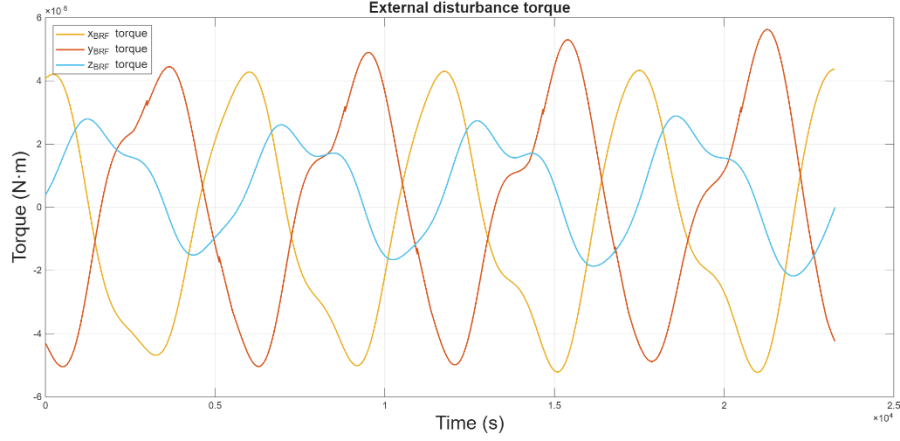
Figure 8: Total environmental disturbance torque on X, Y, Z axes of BRF

5. Results

5.1. Configuration with no gyroscopes

The performance of the ADCS is first presented without taking into account the measurements provided by the gyroscopes. Figure 9 and Figure 10 show the σ values of α, β, γ estimations obtained as the square roots of the first three diagonal elements of the covariance matrix $\underline{\underline{P}}$. It has been observed that the σ values are coherent with the angular estimation errors, which are equal to $0.02°$ for roll, $0.03°$ for pitch and $0.05°$ for yaw in nominal conditions.
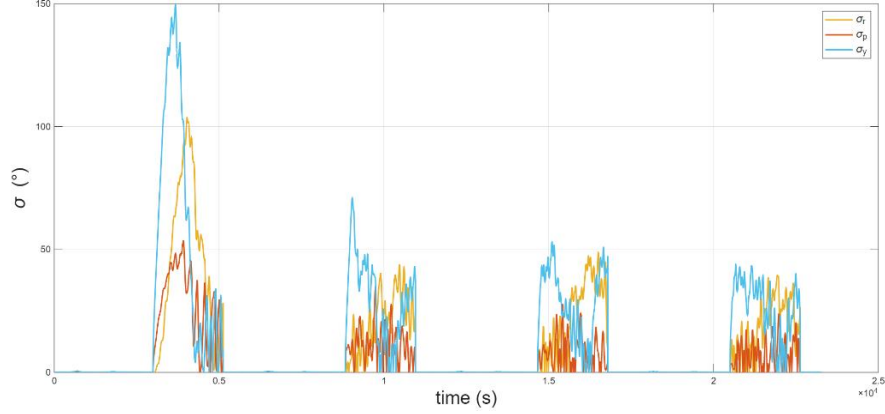
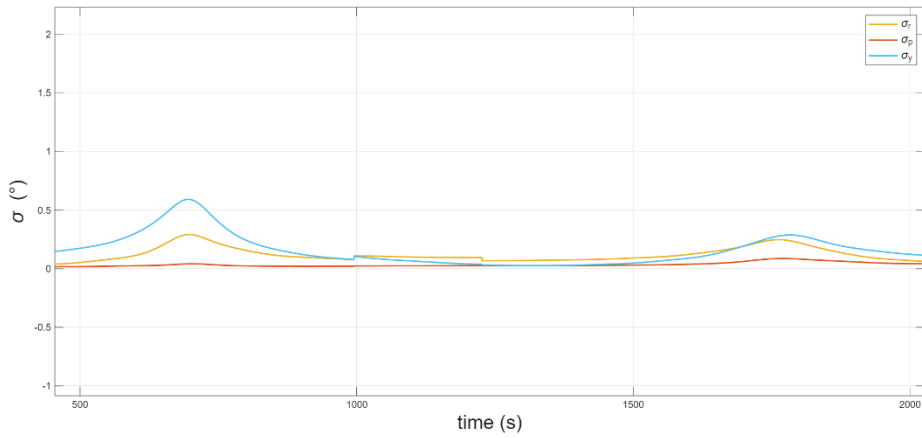*Figure 9: σ values for roll, pitch and yaw in 4 orbits*

Figure 10: Zoomed σ values for roll, pitch and yaw

It can be observed that sigma values undergo rapid increases during 4 intervals, which coincide with the eclipses, however there are peaks also during the daylight periods, as during those time intervals the angle between the Sun direction $\underline{\hat{S}}$ and the magnetic field direction $\underline{\hat{B}}_0$ decreases to about 5°-10°. When this occurs, the angular separation between $\underline{\hat{B}}_0$ and z_{BRF} is smaller than that with the other two axes. As a result, the sigma of the yaw angle σ_y is higher compared to those of pitch and roll. It is evident that the filter is unable to estimate the attitude during eclipse periods. In particular, rotations around $\underline{\hat{B}}_0$, which is the only measured direction, cannot be estimated. This is especially clear when observing the peaks in the angular sigmas during eclipses, which correspond to the time instants when the separation between the corresponding axis and $\underline{\hat{B}}_0$ is minimum.

As for the controller, the initial attitude is set to the nominal one, meaning that the BRF is aligned with the ORF. Using the gain values indicated in Section 3, the evolution of the roll, pitch, and yaw angles is shown in Figure 11.
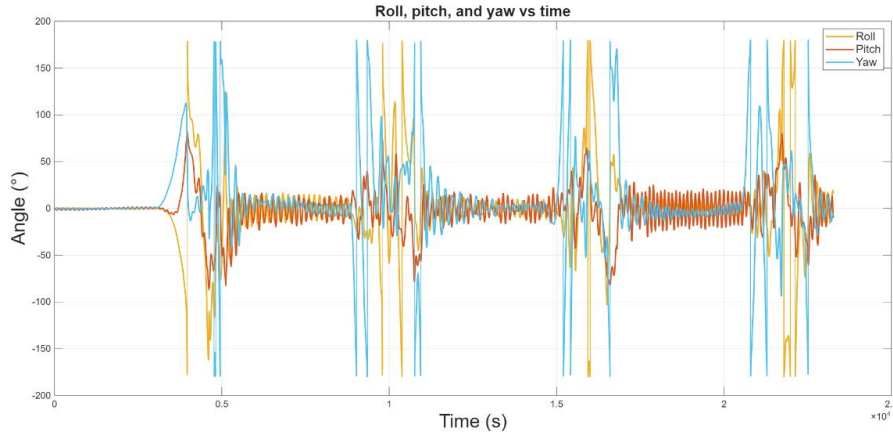

Figure 11: Evolution of roll, pitch and yaw angles without gyroscopes

During the first orbit, before entering eclipse, the controller maintains an error with respect to the nominal attitude of less than 1 degree for roll, 2 degrees for pitch, and less than 1 degree for yaw. As soon as the satellite enters eclipse, roll and pitch remain within these bounds for 300 seconds, while yaw stays within the range for approximately 100 seconds.

In the illuminated phases following the first eclipse, the attitude error stabilizes around several tens of degrees for roll, pitch, and yaw, but does not diverge. These errors, however, are not acceptable for EO missions. To improve the attitude estimation and enhance ADCS performance, the gyroscopes are introduced.

5.2. Configuration with gyroscopes

The addition of the gyroscopes significantly improve the performance of the MEKF. It is observed that the highest sigma value for all three axes occurs during eclipse and reaches at most 0.08°, only for the yaw axis, while roll and pitch show even lower values (Figure 12).
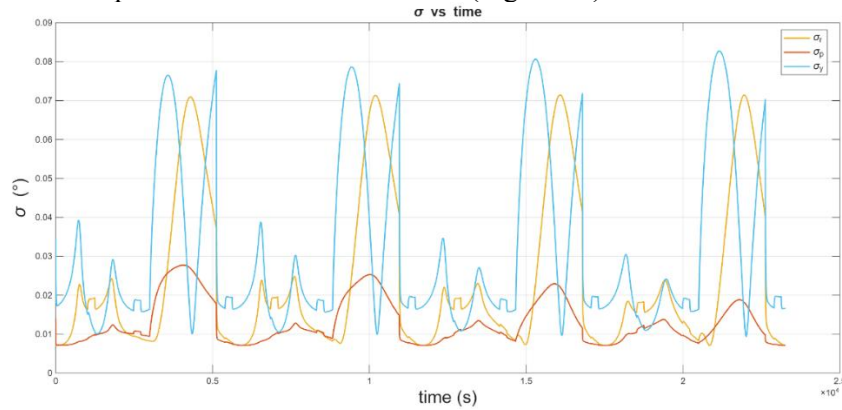

Figure 12: σ values for roll, pitch and yaw in 4 orbits with gyroscopes

The estimation errors for roll, pitch, and yaw reach maximum values of approximately 0.25, 0.09, and 0.2 degrees, respectively, during eclipse. In nominal conditions, the errors drop to about 0.015, 0.02, and 0.02 degrees, which is consistent with the angular sigma values (Figure 13).
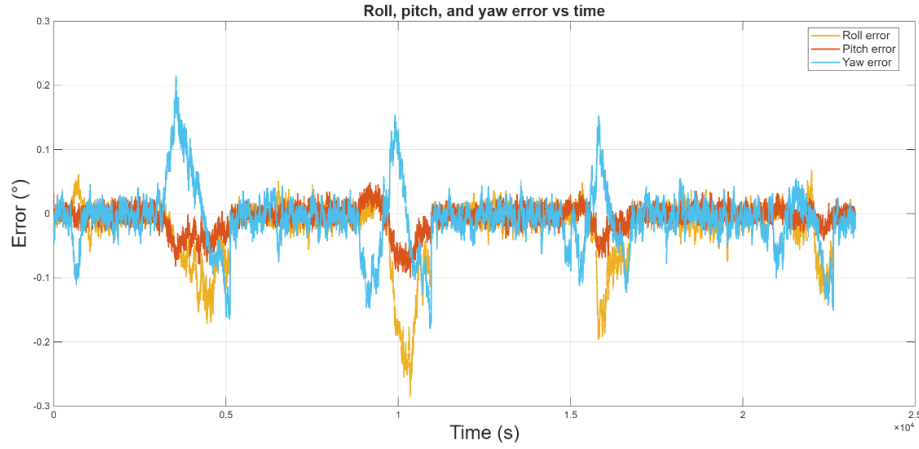

Figure 13: Angular estimation errors of roll, pitch and yaw angles with gyroscopes

These estimation performances are clearly better than in the previous case, thanks to the inclusion of gyroscope measurements.

The controlled dynamics maintains a maximum deviation from the nominal attitude of 0.25 degrees for roll, pitch, and yaw, observed during eclipse, the deviation from the nominal attitude is on the order of 0.1 ° during the nominal phase (Figure 14). These values are acceptable for an EO mission such as PREFIRE.
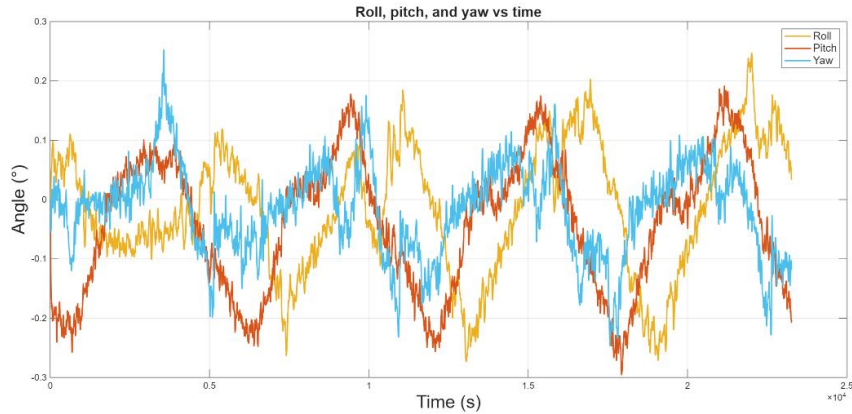

Figure 14: Evolution of roll, pitch and yaw angles with gyroscopes

Since the controller receives the estimated attitude from the MEKF as input, a more accurate attitude estimate leads to more effective control.

The low-frequency oscillations in the attitude can be reduced by adjusting the proportional gain. However, doing so results in a higher maximum error that tends to grow over time, which may be unacceptable for an EO mission.

6. Conclusions

This study provides a comprehensive simulation analysis of a 6U CubeSat's ADCS, emphasizing performance under eclipse conditions. Two configurations have been assessed: one without gyroscopes and another incorporating gyroscopes measurements. The gyroscope-less configuration results in notable performance deterioration, with attitude estimation errors reaching tens of degrees, critically impacting EO mission capabilities. In contrast, including gyroscopes substantially enhanced ADCS performance, maintaining angular deviations below 0.25 degrees, even during prolonged eclipse phases. These results confirm that gyroscopes improve the robustness of the ADCS in the presence of sensor

outages, maintaining the pointing accuracy required by EO missions. Future studies could focus on refining the RWs model to account for dynamic imbalances and viscous friction effects, enhancing sensor simulations by considering partial occlusions due to satellite appendages, and exploring alternative control strategies, such as Quaternion Feedback Regulators (QFR) or the inclusion of integral control components.

7. Bibliography

[1] K. Mmopelwa, T.T. Ramodimo, O. Matsebe, B. Basutli, Attitude determination system for a CubeSat experiencing eclipse, Sensors 23 (2023) 8549. https://doi.org/10.3390/s23208549

[2] K. Dahia, N. Horri, C. Musso, N. Merlinge, Gyroless satellite attitude determination using a SVD-Laplace Particle Filter, Acta Astronautitca. 207 (2023) 33–46. https://doi.org/10.1016/j.actaastro.2023.04.006

[3] C. Hajiyev, D. Cilden-Guler, Gyroless nanosatellite attitude estimation in loss of sun sensor measurements, IFAC-PapersOnLine 51 (30) (2018) 89–94. https://doi.org/10.1016/j.ifacol.2018.11.395

[4] J.R. Cordova Alarcon, M.A. Mendoza, A. Solis-Santome, Attitude determination system based on vector observations for satellites experiencing sun–eclipse phases, in: Proc. of the 4th International Workshop on Satellite Constellations and Formation Flying, October 2014, DOI: 10.1007/978-3-319-09595-6_8

[5] Students' Space Association, PW-Sat2 Critical Design Review: Attitude Determination and Control System, Warsaw University of Technology, November 2016, Issue no. 1

[6] T. S. L'Ecuyer, B. J. Drouin, J. Anheuser, M. Grames, D. S. Henderson, X. Huang, B. H. Kahn, J. E. Kay, B. H. Lim, M. Mateling, A. Merrelli, N. B. Miller, S. Padmanabhan, C. Peterson, N.-J. Schlegel, M. L. White, and Y. Xie, "The Polar Radiant Energy in the Far Infrared Experiment: A New Perspective on Polar Longwave Energy Exchanges," Bulletin of the American Meteorological Society, vol. 102, no. 7, pp. E1431–E1449, 2021. DOI: 10.1175/BAMS-D-20-0155.1

[7] CubeSpace Satellite Systems, CubeSense Sun Gen 2 – Product Description, Version 1.00, 26 July 2023. Document No. CS-DEV.PD.CS-01

[8] CubeSpace Satellite Systems, CubeMag Gen 2 – Product Description, Version 1.01, 9 January 2024. Document No. CS-DEV.PD.CM-01

[9] AAC Clyde Space, PG400 Gyroscope, [Online]. Available: https://www.aac-clyde.space/what-we-do/space-products-components/adcs/pg400-gyroscope.

[10] CubeSpace, GEN 2 ADCS Actuators – Product Overview Brochure, [Online]. Available: https://www.cubespace.co.za.

[11] NewSpace Systems, Magnetorquer Rod [Online]. Available: https://www.newspacesystems.com.

[12] Franquiz, F. J. (2015). Attitude Determination & Control System Design and Implementation for a 6U CubeSat Proximity Operations Mission (Master's thesis). Embry-Riddle Aeronautical University. https://commons.erau.edu/edt/266

[13] . M. Picone, A. E. Hedin, D. P. Drob, and A. C. Aikin, "NRLMSISE-00 empirical model of the atmosphere: Statistical comparisons and scientific issues," *submitted to Journal of Geophysical Research*, Dec. 2001.

[14] J. R. Wertz and W. J. Larson, Eds., *Space Mission Analysis and Design*, 3rd ed. El Segundo, CA: Microcosm Press and Kluwer Academic Publishers, 2003.

[15] N. W. Peddie, International Geomagnetic Reference Field: The Third Generation, J. Geomagn. Geoelectr. 3.